PHYSICAL REVIEW E **70**, 025202(R) (2004)

Preparation of subharmonic patterns in nematic electroconvection

Thomas John and Ralf Stannarius
Fakultät für Naturwissenschaften, Institut für Experimentelle Physik I, Universität Magdeburg, Universitätsplatz 2, D-39106 Magdeburg, Germany

(Received 10 March 2004; published 31 August 2004)

Nematic electroconvection is studied under asymmetric periodic excitation with a driving electric field $E(t)=E(t+T)\neq -E(t+T/2)$. A new dynamic regime, distinguished by subharmonic dynamics, is discovered in the pattern state diagram between conventional conductive and dielectric regimes. The spatial and temporal pattern characteristics are investigated experimentally. The dynamics, threshold fields, and selected pattern wavelengths at onset, calculated from a Floquet analysis of the linearized electrohydrodynamic equations with a test mode ansatz, are in good agreement with experimental results.

DOI: 10.1103/PhysRevE.70.025202 PACS number(s): 05.45.−a, 47.54.+r, 47.20.−k, 61.30.−v

We study the dynamic response of a classical dissipative pattern-forming system, electrohydrodynamic convection (EHC) in nematics, to time-periodic excitation. The linearized dynamic equations in such a system provide information about the stability of the (uniform) ground state. Floquet analysis is a standard tool for the characterization of periodically driven dynamic systems, it yields the asymptotic stability of time-periodic solutions. If one of the Floquet multipliers, depending upon the control parameters, passes +1, a harmonic response in the system variables is expected. If it passes −1, the response is subharmonic. It has been shown that in a large class of systems, symmetric excitation [$A(t)=A(t+T)=-A(t+T/2)$, e.g., driving with sine or square waves of amplitude A and period T], suppresses subharmonic dynamics [1,2].

EHC represents a canonical system in dissipative pattern formation. Recent topics of interest include, among others, aspects of spatial symmetry breaking, localized states, or effects of low dimensionality [3]. The easy manipulation of control parameters, convenient time scales, and straightforward observation techniques, among other advantages, have triggered its comprehensive investigation in the past (for a review, see e.g., Ref. [4]). Above a critical driving voltage, the Carr Helfrich mechanism [5] leads to spatially periodic director deflections $\tilde{\varphi}$ out of the alignment direction x in a planar nematic cell. They are coupled to a periodic modulation of the electric charge density $\tilde{q}$ in the cell plane. Striped patterns appear as the first instability in most cases. They can be described by a test mode ansatz

$$\tilde{\varphi}(x,z,t) = \varphi(t)\cos(k_x x)\cos(k_z z),$$

$$\tilde{q}(x,z,t) = q(t)\sin(k_x x)\cos(k_z z). \qquad (1)$$

Coordinates x, y are in the cell plane, z is along the cell normal. The choice of $k_z=\pi/d$ satisfies the planar anchoring at the glass plates, $\tilde{\varphi}(x,\pm d/2,t)=0$, where d is the cell gap, and $k_x=2\pi/\lambda_{dir}$ reflects the spatial period λ_{dir} of the director deflection pattern. At the conventional sine or square-wave single-frequency excitation, the symmetry of the coupling of the two system variables (q,φ) leads to two observable regimes (Fig. 1), distinguishable by the dynamics of $q(t)$ and $\varphi(t)$. In the low-frequency (conductive) regime, the charge density $q(t)$ alternates with the excitation, the director deflection preserves its sign. In the high-frequency (dielectric) regime, the situation is reversed, $\varphi(t)$ alternates with the excitation (see, e.g., time-resolved observations in [6,7]), and $q(t)$ keeps its sign. In the conductive regime, similar to other convective instabilities, the selected wave number $k_{th}\approx\pi/d$ is essentially determined by the container dimension. In the dielectric regime, k_{th} is usually much higher, depending on viscous, elastic, and electric material properties. Both regimes are well separated at the cutoff frequency f_c, usually with a jump of k_{th}. So far, no subharmonic patterns have been reported in nematic EHC [8].

In our experiments, the cell gap is $d=20.2$ μm. Planar director alignment along x is achieved by a polyimid coating of the glass and rubbing. A fixed sample temperature of 30 °C is controlled with a Linkam TMS 600 hot stage. The mesogenic material *Mischung 5*, a mixture of phenylbenzoate derivatives [9], is nematic from room temperature to 70.5 °C. Most of the involved material parameters are known

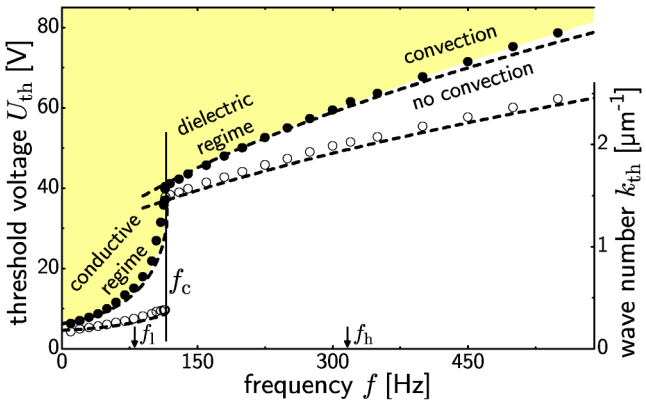

FIG. 1. Measured threshold voltages (●) and selected wave numbers (○) for EHC at a single-square-wave excitation. The cell gap is 20.2 μm. At the cutoff frequency $f_c=115$ Hz, the selected wave number jumps from 0.4 to 1.5 μm^{-1}. The calculated threshold voltages and wave numbers (---) correspond to the (global) minimum of the neutral curves determined from a linear stability analysis of the electrohydrodynamic equations.

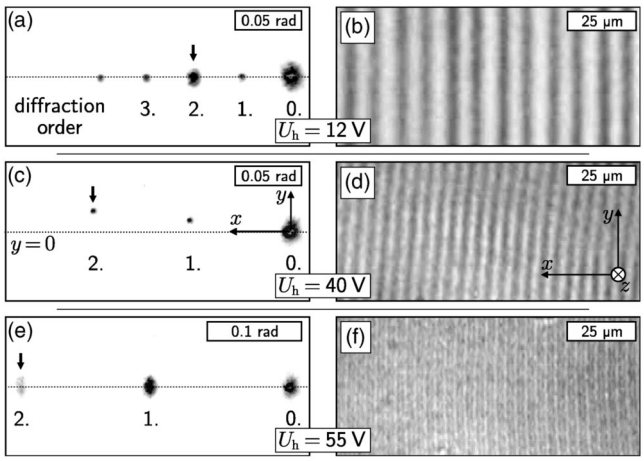

FIG. 2. Laser diffraction patterns (a),(c),(e) and microscope images (b),(d),(f) observed at in-phase superposition of two square waves, (f_l=80 Hz$<f_c<f_h$=320 Hz), for three representative voltages U_h. The amplitude U_l is chosen immediately above the threshold $U_{l,\mathrm{th}}$ for the onset of convection. In the subharmonic regime (c),(d) the pattern is slightly oblique already at onset. Arrows in the diffraction images mark the positions of the photodiode used for the recording of the trajectories shown in Figs. 4(a), 5(a), and 6(a). Only one wing of the symmetric diffraction image is shown.

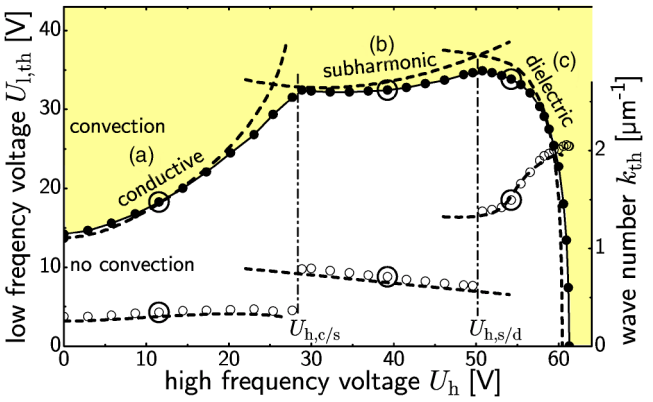

FIG. 3. Measured threshold voltages for the pattern onset (●) and selected wave numbers (○) for in-phase superposition of f_l =80 Hz and f_h=320 Hz square waves. The convection-free ground state is surrounded by a conductive (a), a subharmonic (b), and a dielectric regime (c). The selected wave numbers jump at the transitions between these regimes. Circles mark the parameters (U_l, U_h) where the images of Fig. 2 have been taken. Dashed lines show calculated thresholds and wave numbers extracted from the (global) minimum of the neutral curve $\mathcal{N}$ in the (U_l, k_x) plane for given U_h (cf. Fig. 7).

from independent experiments. Some unknown parameters, like the conductivity that varies slightly for individual cells, were determined by fitting threshold voltages and wave numbers at single-frequency square-wave excitation to the measured characteristics [10,11]. In detail, $\varepsilon_\parallel$=5.6, $\varepsilon_\perp$=6.0, $\sigma_\parallel$ =260 s^{-1}, $\sigma_\parallel/\sigma_\perp$=1.5, α_1=0.2 g cm^{-1} s^{-1}, $\gamma_1=-\gamma_2$ =3.67 g cm^{-1} s^{-1}, η_1=4 g cm^{-1} s^{-1}, η_2=0.4 g cm^{-1} s^{-1}, $K_{11}=14.9\times10^{-7}$ g cm s^{-2}, $K_{33}=13.76\times10^{-7}$ g cm s^{-2} (cgs units). The pattern dynamics is recorded using laser diffraction [11]. The He–Ne laser beam (wavelength λ_L =632.85 nm) is diffracted by phase and amplitude gratings formed by the periodically distorted director field.

In order to simplify the determination of Floquet multipliers in the theoretical stability analysis, it is advantageous to split the excitation wave form into piecewise constant parts [12]. In this paper, we generate an asymmetric wave form $U(t)=U(t+T)\neq -U(t+T/2)$ of the excitation voltage U by superposition of two commensurate square waves without phase shift [13]: a low-frequency ($f_l<f_c$) square wave with amplitude U_l, and a high frequency ($f_h=4f_l>f_c$)) square wave with amplitude U_h [see graphs in Figs. 4(b), 5(b), and 6(b)]. The experiments show that this has considerable consequences for the dynamics of the system variables and the selected wavelength. A subharmonic regime is discovered both in experiment and numerical simulations. When f_h is not an even multiple of f_l, or at a certain phase shift of the two frequencies, the subharmonic regime disappears from the pattern stability diagram. Qualitatively, the same effects are found for other asymmetric wave forms or even at simple sawtooth excitation. We focus on piecewise constant excitation wave forms here, because they allow to integrate the dynamic equations analytically.

Figure 2 shows typical diffraction images, taken slightly above the threshold voltage $U_{l,\mathrm{th}}$ for pattern onset (see, Fig. 3), compared to microscope images at the same driving parameters. The particular values of U_h were chosen to portray the conductive [Figs. 2(a) and 2(b)], subharmonic [Figs. 2(c) and 2(d)], and dielectric [Figs. 2(e) and 2(f)] regimes. A full period λ_{dir} of $\tilde{\varphi}$ and $\tilde{q}$ corresponds to two dark/bright stripe pairs in Figs. 2(b) and 2(d), but to one stripe pair in Fig. 2(f) [7]. Fast intensity modulations due to the oscillation of $\varphi(t)$ are averaged by the camera. The charge field is not accessible with this setup, but owing to the coupling between $\tilde{q}$ and $\tilde{\varphi}$, the director deflection mode $\varphi(t)$ provides sufficient information to characterize the pattern amplitude dynamics.

The diffraction angle θ_n of the nth-order reflex corresponds to the wave number $k_x=2\pi \sin\theta_n/(n\lambda_L)$. An analysis of light propagation in periodic weakly distorted director fields yields an intensity $I_n(t)\propto\varphi(t)^{2n}$ of even order reflexes, originating mainly from the phase grating [11]. Odd order reflexes, essentially caused by the amplitude grating, are more complexly related to the director deflections. Therefore, we extract the pattern dynamics from the intensity of the second-order reflex, $I_2(t)\propto\varphi(t)^4$.

The stability diagram in the (U_l, U_h) plane is shown in Fig. 3. The experimental thresholds are determined by slowly increasing U_l at fixed U_h. At the transitions between the regimes, the selected wave numbers jump discontinuously. More important, however, is the change of the temporal characteristics of $\varphi(t)$. Figures 4(a), 5(a), and 6(a) depict $I_2(t)$ at the positions marked by arrows in Fig. 2; they have been normalized to the same maximum. In addition, the excitation wave form and calculated $\varphi(t)$ and $q(t)$ (see below) are shown in the bottom part (b) of each figure.

For calculation of the onset of EHC, we analyze the stability of the linearized electrohydrodynamic equations [4,14] with the mode ansatz of Eq. (1). This reduces the dynamic model to a system of two coupled ordinary differential equations in the system variables,

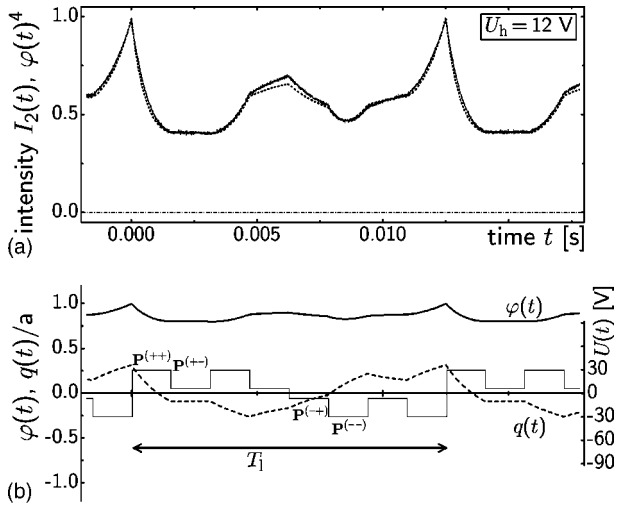

FIG. 4. (a) Normalized intensity $I_2(t)$ [—in (a)] with the same excitation parameters as in Fig. 2(a) and 2(b), measured with a photodiode. (b) Excitation wave form, calculated $\varphi(t)$ [in (rad), solid line], and calculated $q(t)$ rescaled with $a = 20\ \mathrm{cm} \times k_{\mathrm{th}}$ [in ($\mathrm{g}^{1/2}\ \mathrm{cm}^{-3/2}\ \mathrm{s}^{-1}$),- - -]. In the calculation, the same U_h, the corresponding theoretical threshold $U_{l,\mathrm{th}} = 18.1$ V, and selected wave number $k_{\mathrm{th}} = 0.3\ \mu\mathrm{m}^{-1}$ have been used. Independent of their initial values, $\varphi(t)$ and $q(t)$ reach the asymptotic dynamics shown after a few periods $T_l = 1/f_l$. Characteristic for the conductive regime, $\varphi(t)$ keeps its sign. The calculated $\varphi(t)^4$ curve [dotted line in (a)] in the top figure is mostly covered by the experimental $I_2(t)$ graph.

$$\frac{\mathrm{d}}{\mathrm{d}t}\vec{z}(t) + \begin{pmatrix} 1/T_q & \sigma_{\mathrm{H}}E(t) \\ aE(t) & \Lambda_1 - \Lambda_2 E(t)^2 \end{pmatrix}\vec{z}(t) = 0, \qquad (2)$$

$\vec{z}(t) = (q(t), \psi(t))^T$, with $\tilde{\psi}(x,z,t) = \partial_x \tilde{\varphi}(x,z,t) \rightarrow \psi(t) = k_x \varphi(t)$. The coefficients are defined in [14] (in the cgs system), they contain material parameters and the wave number k_x of the respective test modes. $E(t) = U(t)/d$ is the electric field strength. For symmetric square or sine wave excitations with

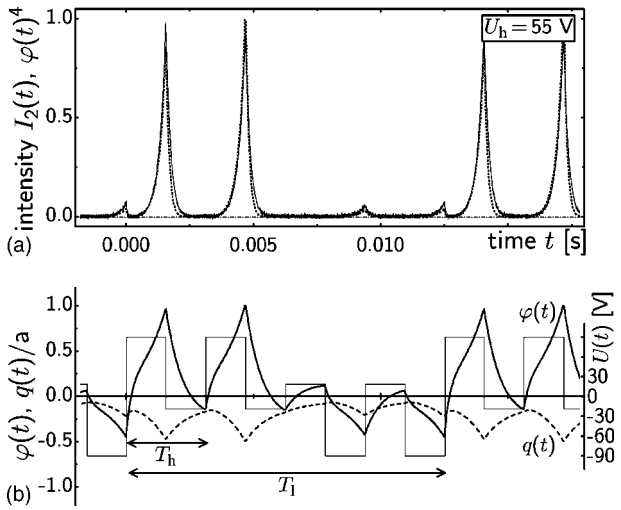

FIG. 5. Same as in Fig. 4, but with parameters of Fig. 2(e) and 2(f), $U_h = 55$ V. Characteristic for the dielectric regime, $\varphi(t)$ alternates its sign with the frequency f_h, the pattern is periodic with T_l.

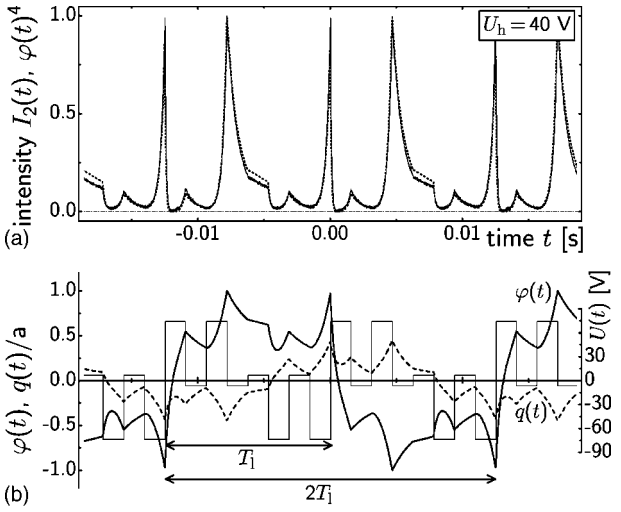

FIG. 6. Same as in Fig. 4, but with parameters of Fig. 2(c) and 2(d), in the subharmonic regime at $U_h = 40$ V. Both $\varphi(t)$ and $q(t)$ are periodic with $2T_l = 2/f_l$, they change sign with period T_l.

amplitude U_{th} and period T, the Floquet analysis predicts asymptotic solutions with period T, as they are found in the common EHC experiment. The asymptotic stability of $\vec{z}(t) \rightarrow \mathrm{e}^{\lambda_1 t}\vec{z}(0)$ is defined by the Floquet exponent $\lambda_1 \in \mathbb{C}$ with the largest absolute real part. The contour of the real part $\mathrm{Re}\{\lambda_1(U,k_x)\} = 0$ defines the neutral curve $\mathcal{N}$, and the global minimum with respect to U of the neutral curve, $(U_{\mathrm{th}}, k_{\mathrm{th}})$, yields the threshold voltage and the selected wave number.

At square-wave excitation, and superpositions of such wave forms, the electrical field is constant between consecutive jumps at t_i and t_{i+1}. During intervals with constant E, Eq. (2) has constant coefficients and the propagation from $\vec{z}(t_i)$ to $\vec{z}(t+t_i)$ is given by a real 2×2 matrix $\mathbf{P}$

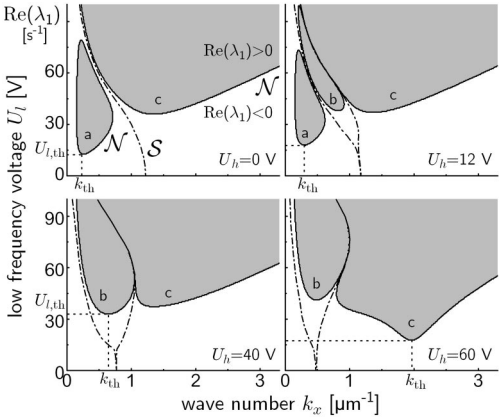

FIG. 7. Density plot of the calculated growth rate $\mathrm{Re}(\lambda_1)$ for the in-phase superposition of 80 and 320 Hz square waves. The threshold voltage $U_{l,\mathrm{th}}$ and selected wave number k_{th} are defined by the global minimum in U_l of the neutral curve $\mathcal{N}$ (—). At $U_h = 0$, regions of the conductive (a) and the dielectric (c) patterns are separated by the singularity $\mathcal{S}(-\bullet-)$, where $\mathrm{Re}(\lambda_1) \rightarrow -\infty$. With increasing U_h, the subharmonic pattern region (b) appears, and when U_h exceeds ≈ 25 V, it provides the global minimum of $\mathcal{N}$. Between the two branches of $\mathcal{S}$, the eigenvalues of the propagator matrix $\mathcal{P}$ are negative, $\mathrm{e}^{\lambda_1 T_l} < 0$. At U_h above ≈ 50 V, the dielectric pattern (c) provides the global minimum of $\mathcal{N}$.

$$\vec{z}(t) = \mathbf{P}(E, k_x, t - t_i)\vec{z}(t_i), \quad t_i \leqslant t \leqslant t_{i+1}. \tag{3}$$

For pure square-wave excitation with period T, the propagation of $\vec{z}(t)$ at $t=nT$ can be expressed by a chain of equal matrix products of $\mathbf{P}^{\sigma}=\mathbf{P}(\sigma E, k_x, T/2)$, $\sigma=\pm 1$,

$$\vec{z}(nT) = [\mathbf{P}^{(-)}\mathbf{P}^{(+)}]^n \vec{z}(0). \tag{4}$$

In the case of an in-phase superposition of two commensurate square waves with $E(t)=\sigma_l E_l+\sigma_h E_h$ and periods T_h and $T_\mathrm{l}=2mT_h, m \in \mathbb{N}$, the propagation is given by products of $\mathbf{P}^{\sigma_l \sigma_h}=\mathbf{P}(\sigma_l E_l+\sigma_h E_h, k_x, T_{h/2})$, $\sigma_{l/h}=\pm 1$

$$\mathcal{P} = [\mathbf{P}^{(--)}\mathbf{P}^{(-+)}]^m [\mathbf{P}^{(+-)}\mathbf{P}^{(++)}]^m \tag{5}$$

$$\vec{z}(nT_\mathrm{l}) = \mathcal{P}^n \vec{z}(0). \tag{6}$$

Equation (3) provides $\vec{z}(t)$ at intermediate times. The Floquet multiplier $\mu_1=\exp(\lambda_1 T_l)$ and the exponent λ_1 follow immediately from the eigenvalue $\mathcal{E}_1$ of $\mathcal{P}$ with the largest absolute value [12], $\lambda_1(U_l, U_h, k_x)=(1/T_l)\ln(\mathcal{E}_1)$. For the pure square wave, both eigenvalues of $\mathbf{P}^{(-)}\mathbf{P}^{(+)}$ are real and positive, and $\vec{z}(t)$ is periodic with T. The same is found for the superimposed fields in regions (a) and (c) of Fig. 7. In the subharmonic regime [(b) in Fig. 7], both eigenvalues are of $\mathcal{P}$ negative but $\mathrm{Re}(\lambda_1) \geqslant 0$.

In summary, a new convection regime with subharmonic dynamics has been discovered. A necessary condition for the appearance of this regime is obviously the asymmetry of the excitation in the two half-periods of the driving field. However, Figs. 4 and 5 prove that this condition is not sufficient. The experimental observations are confirmed quantitatively by a Floquet analysis of the linearized dynamic model equations. The wave number of the subharmonic pattern depends on both superimposed frequencies; the choice of these frequencies allows us to produce convection patterns in a continuous range of wavelengths, between those of the conduction and dielectric regimes. Preliminary results show that the wave number decreases with increasing container dimensions, but is weaker than in the conduction regime. It is interesting to compare these results with other dissipative pattern forming systems. In the Faraday instability, the typically primary pattern is subharmonic, but in two-frequency forcing, a couple of new pattern structures have also been observed [15]. Subharmonic response has also been described in the periodically forced oscillatory Belousov-Zhabotinsky reaction [16], or for the parametrically driven pendulum [17].

The authors particularly acknowledge Jana Heuer and Fabian Senf, who found the experimental evidence of the subharmonic EHC patterns. Ulrich Behn is acknowledged for stimulating discussions.

[1] T. P. Schulze, Phys. Fluids **11**(12), 3573 (1999).

[2] J. W. Swift and K. Wiesenfeld, Phys. Rev. Lett. **52**, 705 (1984).

[3] E. Plaut, W. Decker, A. G. Rossberg, L. Kramer, W. Pesch, A. Belaidi, and R. Ribotta, Phys. Rev. Lett. **79**, 2367 (1997); M. Dennin, G. Ahlers, and D. S. Cannell, *ibid.* **77**, 2475 (1996); J.-H. Huh and S. Kai, Phys. Rev. E **68**, 042702 (2003). T. Peacock, D. J. Binks, and T. Mullin, Phys. Rev. Lett. **82**, 1446 (1999).

[4] L. Kramer and W. Pesch, Annu. Rev. Fluid Mech. **17**, 515 (1995); L. Kramer and W. Pesch, in *Pattern Formation in Liquid Crystals* (Springer, New York, 1995).

[5] E. F. Carr, J. Chem. Phys. **38**, 1536 (1963); W. Helfrich, *ibid.* **51**, 4092 (1969); E. Dubois-Violette, P. G. de Gennes, and O. Parodi, J. Phys. (Paris) **32**, 305 (1971).

[6] U. Schneider, M. de la Torre Juárez, W. Zimmermann, and I. Rehberg, Phys. Rev. A **46**, 1009 (1992).

[7] H. Amm, M. Grigutsch, and R. Stannarius, Z. Naturforsch., A: Phys. Sci. **53a**, 117 (1998).

[8] However, a subharmonic regime had been predicted theoretically (but not been found in experiments so far) for EHC in ferroelectric smectic C^* films, where the spontaneous polarization is a symmetry-breaking element; see S. Ried, H. Pleiner, W. Zimmermann, and H. Brand, Phys. Rev. E **53**, 6101 (1996).

[9] H. Amm, R. Stannarius, and A. Rossberg, Physica D **126**, 171 (1999).

[10] T. John, U. Behn, and R. Stannarius, Phys. Rev. E **65**, 046229 (2002).

[11] T. John, U. Behn, and R. Stannarius, Eur. Phys. J. B **35**, 267 (2003).

[12] C. S. Hsu, J. Math. Anal. Appl. **45**, 234 (1974).

[13] All positive slopes of the low-frequency square wave coincide with positive slopes of the high-frequency square wave.

[14] U. Behn, A. Lange, and T. John, Phys. Rev. E **58**, 2047 (1998).

[15] T. Besson, W. S. Edwards, and L. S. Tuckerman, Phys. Rev. E **54**, 507 (1996).

[16] A. L. Lin, A. Hagberg, A. Ardelea, M. Bertram, H. L. Swinney, and E. Meron, Phys. Rev. E **62**, 3790 (2000).

[17] E. I. Butikov, J. Phys. A **35**, 6209 (2002).